

Research Paper

Comparison of cooling plate configurations for automotive battery pack thermal management

K. Darcovich^{a,*}, D.D. MacNeil^a, S. Recoskie^a, Q. Cadic^b, F. Ilinca^c^a National Research Council of Canada, Energy, Mining and Environment Research Centre, Ottawa, Ontario K1A 0R6, Canada^b ICAM-Toulouse, 75 Avenue de Grande Bretagne, 31300 Toulouse, France^c National Research Council of Canada, Automotive and Surface Transportation Research Centre, Boucherville, Québec J4B 6Y4, Canada

HIGHLIGHTS

- Novel 3D electrochemical model with heat generation, gives thermal field in prismatic cells.
- investigated Ice plates (flush with cell face) and Cold plates (bottom surface of cell)
- Thermal profiles found as function of drive cycle, cooling regime and battery case material.
- Ice plates give thermal rises 5–8 K less than Cold plate, and provide narrower ΔT range
- among battery case materials tested, Cold plate cooling is best with thick aluminum

ARTICLE INFO

Keywords:
 Battery simulation
 Prismatic cell
 Cooling plates
 Drive cycles
 Lifetime estimates

ABSTRACT

A numerical simulation was developed combining micro and macro scale models, to determine the thermal state of battery packs in electric vehicles. A spatially resolved Ohm's law model was integrated with the single particle model to resolve the electrochemistry in prismatic cells, and then coupled with a thermal transport simulation. The objective was to compare the effectiveness of two types of liquid channel cooling plate configurations. The first, known as ice plates are placed between every second cell in the battery pack. The second, known as cold plates, are placed underneath a block of cells, and absorb heat only through the small lower face of the cell, exploiting anisotropic heat transfer properties. In general, the ice plate performs better. The cold plate is less complicated and expensive to integrate into the battery pack, and has more scope for higher coolant circulation rates. This paper compares the performance of the two cooling systems, highlighting the conditions where each system works best, along with quantitative assessments obtained through numerical simulation.

1. Introduction

At this time, electric vehicle technology is advancing at a rapid pace, giving them a steadily increasing market share. Principal areas of technical attention are energy capacity, power delivery and environmental concerns [1,2]. Some main consumer concerns include on-road performance, vehicle safety and a reliable driving range. All of these factors have an impact on the vehicle battery pack. These collective efforts are making it apparent that progress with any of these technical challenges could be assisted with effective thermal management in the battery pack. In particular, for the automotive sector, high power demands coupled with volume constraints inside the vehicle place a premium on thermal management. At the same time, from early stage competition to secure market share, battery stability and longevity are

achieved with oversized, and only partially exploited battery packs, operating under conservative battery management (BMSs) control systems, and some degree of active or passive cooling. [3,4] In this context, the present work is focussed on exploring some options for thin channel fluid-circulating plate cooling systems.

A general overview of the emerging body of technical literature treating battery pack cooling was presented in [5–7]. The papers referenced and subjects discussed there covered a diverse range of technical systems, such as passive air, forced air and circulating liquid plate cooling, and thermal generation from batteries. In [7], a summary of liquid plate battery cooling was given, citing effective performance, small thermal gradients even at elevated currents, and a comparatively high operational energy requirement. These represented initial research efforts, so typically battery function, or cooling function or both were

* Corresponding author.

E-mail address: ken.darcovich@nrc-cnrc.gc.ca (K. Darcovich).

Nomenclature			
c_p	heat capacity in Eq. (6) ($\text{J kg}^{-1} \text{K}^{-1}$)	κ_{SEI}	electric conductivity SEI film (S/m)
E_{0s}	side reaction activation energy (J/mol)	η	overpotential in SPM (V)
F	Faraday constant = 28.601 (Ah/mol)	η_s	side reaction overpotential from [41] (V)
h	heat transfer coefficient in Eq. (7) ($\text{W m}^{-2} \text{K}^{-1}$)	ρ	density in Eq. (6) (kg/m^3)
h_c	heat transfer coefficient in Fig. 4 for active cooling context ($\text{W m}^{-2} \text{K}^{-1}$)	ρ_{SEI}	density of SEI layer (kg/m^3)
h_p	heat transfer coefficient in Fig. 4 for passive cooling context ($\text{W m}^{-2} \text{K}^{-1}$)	$\sigma_{\text{el}}^{\text{eff}}$	effective electrode conductivity (S/m)
I_{el}	current in electrode (A)	$\sigma_{\text{io}}^{\text{eff}}$	effective electrolyte conductivity (S/m)
I_{io}	current in electrolyte (A)		
J	Kim model current source term, equivalent to intercalation current density in SPM (A/m^2)		
J_i	intercalation current density in SPM (A/m^2)		
J_s	degradation current density (A/m^2)		
k	thermal conductivity in Eq. (7) ($\text{W m}^{-1} \text{K}^{-1}$)		
k_{0s}	side reaction rate constant (A/m^2)		
L_{SEI}	SEI layer thickness (m)		
M_{SEI}	molar mass of SEI material (kg/mol)		
n	unit outward normal (m)		
Q_{ohm}	resistive heat source (W/m^3)		
Q_{rev}	reversible entropic reaction heat (W/m^3)		
Q_{rxn}	heat source from intercalation reactions (W/m^3)		
Q_{tot}	sum of thermal sources (W/m^3)		
r_n	anode resistance in Eq. (1) (ohm)		
r_p	anode resistance in Eq. (1) (ohm)		
R	universal gas constant = 8.3144 (J/(mol K))		
t	time (s)		
T	temperature (K)		
T_{∞}	external ambient cooling temperature (K)		
V_n	anode potential in Eq. (1) (V)		
V_p	cathode potential in Eq. (2) (V)		
<i>Greek letters</i>			
κ^{eff}	thermal conductivity inside battery ($\text{W m}^{-1} \text{K}^{-1}$)		
<i>Abbreviations</i>			
		BMS	battery management system
		DOD	battery depth of discharge
		EC	ethylene carbonate
		EOL	(battery) end-of-life
		SEI	solid-electrolyte interface
		SOC	battery state-of-charge
		SOH	battery state-of-health
		SPM	single-particle model
<i>Subscripts</i>			
		eff	effective property, for heterogeneous phase
		i	electrode, can be n or n below
		loc	pertaining to local compute cell
		n, neg	anode, negative electrode
		ohm	resistive contribution to heating
		p, pos	cathode, positive electrode
		rev	reversible heat of reaction component
		rxn	electrochemical heating component
		sep	separator layer
		1	electrode phase
		2	electrolyte phase

represented in simplified ways [8–10], to be able to demonstrate basic trends and effects. Up to recently, comprehensive projects which integrate the combined effects of power demands, electrochemical based battery performance, thermal generation, heat transfer and battery cell ageing have been few. Papers leading to the present context outline the development of the components of the numerical approach used here [5,6]. Related efforts at coupling electrochemical and thermal models have been recently made with LiFePO₄ prismatic cells [11], and applied to pack contexts with liquid cooling, simulated at a number of ambient temperatures and current levels [12].

The importance of battery cooling and temperature control is clearly understood, but at present, even the thermal behaviour of the batteries themselves remains a subject of study. There are a number of different cooling concepts possible, such as passive convective systems, forced air systems, immersion cooling and systems with cooling plates. This present study concerns itself with plate systems, and in particular, how they interact with the cells in the battery pack. On the research side, there have been a number of projects focussed on the design and performance of cooling plates (ice plate type) that are inserted between prismatic cells. A main interest is the temperature uniformity obtained in the cell, with simulations performed on plate flow channels with simplified thermal generation models [13], or more sophisticated electrochemically driven thermal inputs across a range of current levels, but with simpler open flow channels between cells [14]. A recent paper [16] has presented an in-depth study of a liquid cooled cold plate system, simulating a small 20 Ah LiNMC cell discharging at a high

current level of 5 C. C-rate is a current value normalizing convention in battery technology, which refers to the constant current level required to discharge a fully charged cell in one hour. In [16], an equivalent circuit battery model was employed, and was used to generate thermal environments to assess cooling performance. These harsh operating conditions created temperature gains of about 13 K, with an internal cell temperature gradient of about 10 K. As the commercial uptake of thin cooling plates becomes more certain, research is now focussing on the geometrical details of the plate flow channels for best prismatic cell cooling performance [15]. There has also been some initial projects on integrated cooling systems, such as one using a Kim-type model with equivalent circuit based electrochemistry, tested with open flow plates and small 715 mA h cells, which reported on operational and design advances which significantly improved temperature distribution uniformity over cell faces [17]. For electrical vehicles with banks of cylindrical batteries, there were two recent studies investigating multi-cell coolant plates designed to fit around banks of 18,650 cells [18,19]. Tests were done for various coolant flow rates and discharge currents. The thermal contact resistance was found to have a very strong impact on performance. The extent of temperature rise using an ice plates cooling system was investigated experimentally on prismatic cells (with lithium phosphate electrodes), then subjecting them to a range of coolant levels for drive cycle demands defined by US06 Supplemental Federal Test Procedure (US06) developed by the US EPA [20].

There is also a very strong commercial interest in this subject of battery pack cooling plates at present, reflected by the amount of

patenting currently taking place. A number of proprietary designs for ice plates for battery cooling are documented in recent patents, by well known companies such as General Motors [21] and Daimler AG [22]. Technology has also been developed for cooling systems with a larger single plate, known as a cold plate or a floor plate. Assignees for cold plate configurations include Ford [23], Jaguar Land Rover [24], and Daimler Chrysler AG [25].

Some efforts have been made to study and characterize the physics and chemistry that drive battery capacity fade. A number of papers focussed on the nature of the degradation mechanisms and their kinetics [1,26], while more applied studies made some attempts to apply the capacity fade models to estimate battery or vehicle lifetimes [27]. Related technology thrusts such as vehicle-to-grid [28,29] and vehicle-to-home [30] are seeking to show the extent of additional battery wear resulting from these supplementary electric vehicle (EV) uses.

This present paper incorporates experimental battery characterization data into a suite of coupled numerical simulations. A number of realistic EV usage scenarios were conceived, and then used as a basis to compare the relative performance and merits of the type of cooling plate system selected, the level of cooling effort applied, as well as material characteristics of the battery cell cases. Performance was demonstrated first by determining battery thermal profiles for the usage scenarios, and then applying these to long term simulations to estimate EV service lives. The modeling approach employed to determine thermal states of prismatic automotive cells under US EPA drive cycles is a recent advance, and its application to a comparative study of cooling plate configurations considered together with various battery case materials, provides the electric vehicle and battery modeling community with novel and insightful results.

2. Model framework

The numerical tools used for this study have the same basis as the simulations that were developed and coordinated in an earlier study [5,6]. For brevity, they will not be developed and explained here, as the full details can be found in [5,6]. To provide at least a basic idea of the modeling approach, the following short outline is offered.

The exchange current that arose during charge or discharge of the battery was determined using the single particle model (SPM) [31–34], which is a simplification of Doyle's original battery transport model [35] from assuming no spatial variation of field values across the widths of the electrode and separator layers in the battery cell. The SPM thus could provide the simulation with values of current, electric potential and lithium ion concentration. The SPM accounts for the electrode morphology as well, incorporating parameters that reflect the grain size, compact porosity and the physical dimensions of the layers.

The SPM terms were then used as a direct means to apply source terms to the Kim model [36–39], which was developed as a two-dimensional two-plate system applying Ohm's law over the geometry of prismatic battery cells to permit a spatially varying current field to be determined.

The basic expressions for the Kim model come from applying Ohm's law over the two domains depicted in Fig. 1, and the following coupled equations result,

$$\nabla^2 V_n = -r_n J \quad (\text{for anode}) \quad (1)$$

$$\nabla^2 V_p = +r_p J \quad (\text{for cathode}) \quad (2)$$

Solving the coupled Eqs. (1) and (2) gives the electrochemical state of a prismatic cell. The local currents which are transferred across the electrode layers are represented by the source terms J (A/m^2), and must also satisfy the Butler–Volmer equation in the SPM, ensuring proper convergence and coherent current fields. The local values of J are of identical magnitude (and opposite sign) for compute cells at the same position of the anode and cathode sheets for each equation.

The original Kim model populated the source terms in Eqs. (1) and

(2) with empirically determined constants that reflected cell reference potentials and cell internal resistances. Through employing the SPM to resolve the electrochemistry, the cell internal resistance can be determined directly for each local point on the prismatic face from model variables. The SPM also makes use of experimentally determined reference potential data, which together with the local cell resistance satisfy all the requirements for the Kim model. Complete details on the formulation and parameters for determining the SPM-based components for the Kim model are given in [5].

The simulations were modeled on a 30 Ah prismatic cell used in a present-day electric vehicle, made with a LiNMC cathode and a graphite anode. The cell electrolyte phase was composed of a mixture of propylene carbonate, ethylene carbonate and dimethylcarbonate [40].

2.1. Capacity fade model

The underlying mechanism responsible for capacity fade is a secondary reaction involving a small amount of lithium which enters the electrolyte phase upon deintercalation during discharge, or intercalation during recharge. Lithium ions in the electrolyte phase react with chemical species present there to form an SEI layer. The mechanism was treated as a simplified single reaction as reported in [41], and incorporated into the battery simulation model. This reaction is an irreversible electrochemical reduction reaction, whose products are deposited in the SEI layer and increase its thickness. This side reaction current density is defined as:

$$J_s = -i_{0s} \exp\left(\frac{-\alpha_c F}{RT} \eta_s\right) \quad (3)$$

The coefficient i_{0s} from Eq. (3) is given an Arrhenius functionality of the form,

$$i_{0s} = k_{0s} \exp\left(\frac{-E_{0s}}{RT}\right) \quad (4)$$

An error minimization technique to find optimal values for k_{0s} and E_{0s} was employed for a large set of cycling simulations compared to experimental measurements. Different values for k_{0s} (A/m^2) and E_{0s} (J/mol) were fitted for charge or discharge modes. Under discharge, k_{0s} was set to 1.17×10^{-5} and E_{0s} was set to 6.60×10^5 , while for charging periods, k_{0s} was set to 3.42×10^{-7} and E_{0s} was set to 5.71×10^5 .

As the secondary reaction proceeds, both the thickness of the SEI layer and its resistance increase according to:

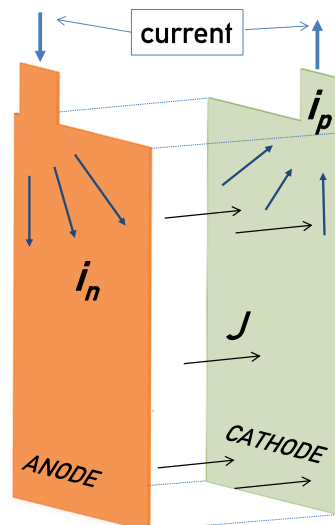


Fig. 1. Schematic of the two coupled electrode domains required for the numerical implementation of the Kim model.

$$\frac{dL_{SEI}}{dt} = \frac{-J_s M_{SEI}}{\rho_{SEI} F} \quad (5a)$$

$$R_{SEI} = \frac{L_{SEI}}{\kappa_{SEI}} \quad (5b)$$

L_{SEI} had an initial value of 5.34×10^{-7} m [5].

Tracking the total amount of lithium consumed by the secondary reaction allows the battery state of health (SOH) to be monitored as the ratio of the amount of lithium remaining in the electrode phases compared to the amount originally present.

2.2. Thermal environment

Energy state changes associated with the battery electrochemistry occurring during charge and discharge produce or consume thermal energy. Details of these mechanisms are given in [42,43], and a discussion of how they were integrated into the model suite employed here was provided in [5,6]. A brief overview of the physical context and the modeling approach is given below.

Normal battery function generates heat according to the mechanisms and physical sectors of the cell as summarized in Fig. 2. Updates of the electrochemical state of the cell with the Kim-SPM approach enable the thermal sources to be determined as a field at each time step and mapped into any accompanying three-dimensional thermal simulation.

The thermal domain representing the prismatic cell structure is modeled according to [44],

$$\rho c_p \frac{\partial T}{\partial t} = \nabla \cdot (\kappa^{\text{eff}} \nabla T) + Q_{\text{ohm}} + Q_{\text{rxn}} + Q_{\text{rev}} \quad (6)$$

For coupling the thermal effects with the electrochemistry, the thermal energy equation is solved in the thermal domain with the source terms from Eq. (6), and with boundary conditions representing the choice of either an ice plate or cold plate cooling system. These configurations are shown in Fig. 3.

The thermal solutions were calculated on a three dimensional domain representing the prismatic cell geometry. Communication between the electrochemical and thermal domains relied on a spatial mapping of the thermal source terms from the electrochemical simulation to the thermal simulation, followed by a mapping in the opposite direction of the temperature field.

For the thermal equation, (Eq. (6)), the following boundary conditions were applied. On the face next to the adjacent battery cell, and on the right, left, top and bottom faces, a thermal zero gradient boundary condition was applied. The middle face was considered a symmetry plane, while the other faces were considered to be insulated, relative to the face next to the cooling plate. The face adjacent to the cooling plate was treated with a convective heat flux condition into a surrounding environment at T_∞ . [45] For this configuration, the boundary condition on the cooled face was given by,

	ANODE	SEPARATOR	CATHODE
Q_{ohm}	$\frac{(I_{\text{el}})^2}{\sigma_{\text{el}}^{\text{eff}}} + \frac{(I_{\text{io}})^2}{\sigma_{\text{io}}^{\text{eff}}}$	$\frac{(I_{\text{el}})^2}{\sigma_{\text{el}}^{\text{eff}}}$	$\frac{(I_{\text{el}})^2}{\sigma_{\text{el}}^{\text{eff}}} + \frac{(I_{\text{io}})^2}{\sigma_{\text{io}}^{\text{eff}}}$
Q_{rxn}	$a j_{\text{loc}} \eta_{\text{loc}}$	0	$a j_{\text{loc}} \eta_{\text{loc}}$
Q_{rev}	$a j_{\text{loc}} T \frac{dU}{dT}$	0	$a j_{\text{loc}} T \frac{dU}{dT}$

Fig. 2. Overview of thermal generation sources in a lithium ion battery.

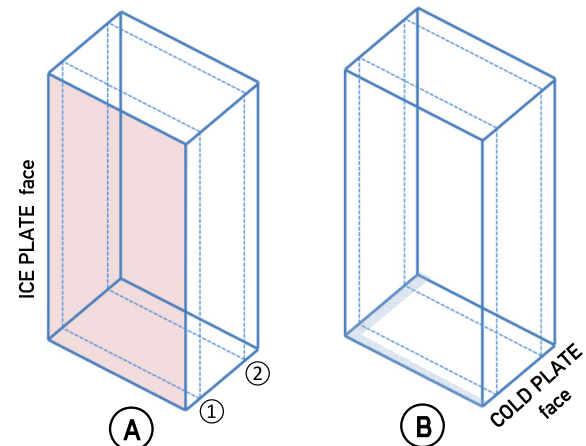


Fig. 3. Schematic of the volume for coupling the Kim-SPM electrochemical battery model with a thermal simulation. (A) shows ice plate configuration. (B) shows cold plate configuration.

$$-k \frac{\partial T}{\partial n} + h(T - T_\infty) = 0 \quad (7)$$

In Eq. (7), the ambient reference temperature was T_∞ and was set to 303 K.

The entire simulation proceeds stepwise by first resolving the electrochemical domain, providing inputs to update the thermal field which in turn updated the temperature field applied to the electrochemical domain.

Table 1 provides a summary of the thermal parameters used here.

Some of the heat transfer parameters have an anisotropic character, attributable to the highly thermally conductive metallic current collector layers in an in-plane orientation, and the comparatively insulating electrode layers oriented out of plane. The 30 Ah cells have main face dimensions of 12.7 by 17.7 mm, they are 5 mm thick, and the polymer pouch case has a thickness of 254 μm .

For the ice and cold plate configurations considered here, in-house thermal analysis of pack arrangements showed that the thermal environment as represented in this paper are very representative for the vast majority of the cells in the pack. Two cells at the pack extremities show temperatures that differ from the pack average by between 0.5 and 1.0 K. The rest of the pack has cell temperatures that vary by less than 0.1 K. While this study was carried out with simulations on a single cell, its results were put into the thermal context of a larger pack, and are very representative of an entire pack.

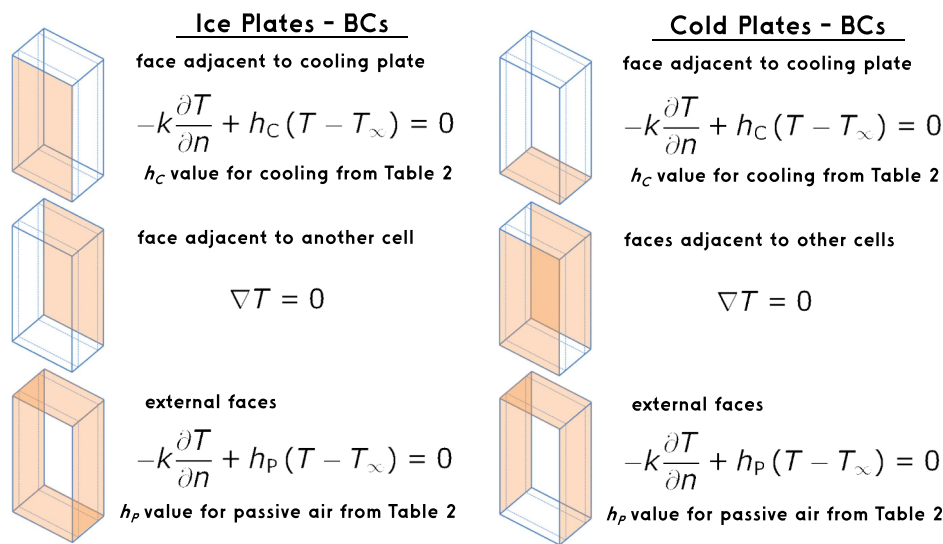


Fig. 4. Prismatic cell ice and cold plate configuration reference for thermal simulation. Boundary conditions from [45].

Table 1

Thermal parameters used in simulations. Electrode properties from [38], polymer case properties measured in house, metal properties from [46].

Parameter	Units	Case material			
		Electrode	Polymer pouch	Aluminum	steel
κ^{eff} (in-plane)	W/(m K)	28.7	55.1		
κ^{eff} (out-of-plane)	W/(m K)	0.881	0.269		
κ^{eff} (isotropic)	W/(m K)			167.0	40.0
ρ	kg/m ³	2780.7	1150.0	2700.0	7832.0
c_p	J/(kg K)	923.2	1900.0	896.0	434.0

3. Experimental

Smaller scale 18650 format cells were selected for experimental measurements for this project in order to provide some battery characteristics for the numerical simulations. Batteries made by LG, a commercial 2200 mA h Lithium-ion (LiNMC, model number ICR18650S3 [47]) were used in cycling tests to refine some parameters used in the models. As outlined more fully in [5,6], cycling tests were done for currents varying from 150 mA up to 1500 mA at 30 °C, and at temperatures from 20 °C to 64 °C at 900 mA current to refine intercalation and capacity loss kinetic parameters, as well as establish the resistive characteristics of the SEI layers. All tests were conducted in a thermally controlled chamber. An exploded diagram of the battery thermal control unit is shown in Fig. 5. The system can operate in a heating or cooling mode, using special thermoelectric module pads (TE Technology, Inc., Traverse City, MI, USA) that can maintain a near constant set point temperature.

In [6] rationale was provided to explain the suitability of performing characterization measurements on 18,650 cells when much larger prismatic cells were simulated in the test performance scenarios. The main points were that the battery chemistries were the same in both cases, and the experiments were performed with strict active temperature control in a test system with very large thermal mass and fine temperature control, which maintained the battery surface temperature to within 0.1 K of the set point given the intimate contact between the large thermal block and the outside cylindrical wall of the 18,650 cell. Reservations expressed in the literature about using characterizations measured from different battery sizes or configurations mainly point out that the thermal environments end up differing [5]. In [5] volumetric thermal generation rates applied to the cells simulated

compared well to thermal gains reported in the literature [8]. In this case, this concern was addressed by cataloguing data at a range of reference temperatures, and then implemented in the simulations as instantaneous temperature values. Battery cycling tests provided parameters for the cell internal resistance and capacity fade rates as a function of temperature, current and cell state of charge. Further, experiments done with small cells are less costly, and much safer.

In lifetime simulations, for periods of time when the battery would be inactive, calendar fade was applied. A calendar life of 16.8 years for cells with the same battery chemistry was reported in the literature and used here [48]. In this case, battery end-of-life was taken to be when the original cell capacity dropped to 75% of its original value.

4. Numerical implementation

The open-source software, OpenFOAM (Field Operation And Manipulation) was used to run the electrochemical-thermal model outlined in Section 2. OpenFOAM is an object-oriented macro-level version of C++, developed for treating systems governed by partial differential field equations [49], especially for work with systems modeling transport phenomena. The electrochemical simulation was performed on two dimensional sheets, and the thermal simulation used a three dimensional body dimensioned according to the 30 Ah prismatic cell considered [5].

Drive cycles developed by the US EPA such as the Urban Dynamometer Driving Schedule (UDDS), Highway (HWY) and US06 were originally used to provide performance characteristics of gasoline

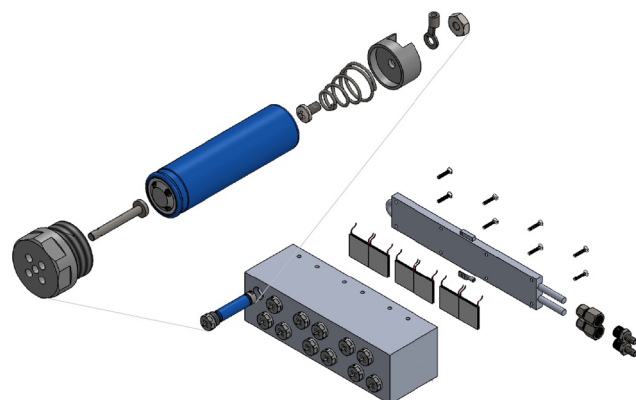


Fig. 5. Thermal control unit for 18,650 battery cell cycling tests.

and diesel fueled vehicles. These standards are now being adopted to for electric vehicles. A drive cycle is a vehicle speed profile over a period of time, such that the power level required to follow the profile reflects the vehicle weight and propulsion system. Scenarios were explored in this work using the HWY and US06 cycles, whose profiles are shown in Fig. 6.

The demand placed on electric vehicle battery packs to adhere to a drive cycle can be estimated with its weight and rolling resistance as inputs [29]. In this study, data taken from a dynamometer for the vehicle considered here with the same prismatic cells was available. Fig. 7 shows the normalized current for one bank of cells as measured on the dynamometer following the US06 drive cycle.

In the present study, an objective was to evaluate and compare ice plate and cold plate cooling configurations under a range of test scenarios including cooling effort and cell case material. The range of simulation parameters explored here are presented in Table 2. For the cases outlined in Table 2, all the parameters were required as inputs to obtain the set of thermal trajectories. Battery lifetime simulations were run for all the parameters outlined, starting from an SOH at 100% and finishing below 75%, making use of upper and lower SOH bounds to provide interpolated thermal trajectories for intermediate SOH values.

5. Results and discussion

The Kim-SPM simulations as described above were run for a number of combinations of parameters to determine the thermal operating environments in the automotive cells to show the combined effects of drive cycle, cooling effort, cooling configuration and the type of battery case material.

The parameters input to the Kim-SPM simulation produced outputs of battery cell temperature profiles which are depicted in Fig. 8 which shows average cell temperatures over the course of 50 km of both US06 and HWY drive cycles, for both air and liquid cooled systems. There are 8 curves shown in plots (a) and (c) in Fig. 8, giving temperature profiles for both ice plates and cold plates, for forced air-cooling, and three levels of liquid-cooling. Plots (c) and (d) give comparisons of the effect of the battery case material for liquid cooled systems for the US06 and HWY drive cycles respectively. Given the significantly more comprehensive face contact of the ice plates, their performance is reflected by substantially lower battery temperatures compared to cold plate cases over the duration of the test simulations shown in Fig. 8.

Recalling the cooling plate configurations illustrated in Fig. 3, it is expected that significant performance differences should result from either ice or cold plate use. Fig. 9 shows the central main-face cross section of a battery cell at the 125 s point from two cases shown in Fig. 8a above for a standard level of liquid cooling. Fig. 9a shows the temperature distribution over a cell cooled by an ice plate, while the temperature field in Fig. 9b is with a cold plate.

Simple observation shows that the ice plate manages to keep the temperature fairly uniform over the cell face, ranging from 304.2 to 304.6 K, while a temperature range of almost 5 K can be seen for the same test conditions cooled by a cold plate. It is also understood that chemical and electrochemical systems function in a very temperature

dependent manner. In general, for the good conservation of battery cells, a uniform current distribution is sought as local regions of higher current will experience greater stress and will degrade more rapidly. The establishment of these kind of spatial non-uniformities leads to a cascading situation where the non-uniformity feeds itself and the local degradation accelerates, potentially leading to material failure. The situation discussed here is illustrated in Fig. 10, taken from the same conditions for the thermal distributions shown in Fig. 9. For the case of current, the total amount is the same in both cases, but it is distributed far more unevenly with cold plate cooling. Compute cell average values are shown here, to avoid a false gradient from the tab areas that would arise with point average shading.

5.1. Effect of system parameters on temperature

Usage scenarios along with cooling systems and level of applied cooling were investigated for their effects on the thermal state of the battery cells. The simulations consisted of 50 km of driving, beginning with a uniform battery temperature of 303 K. The cooling effort is in effect at all times. The cooling level, with the smallest value at $h = 35 \text{ W}/(\text{m}^2 \text{ K})$ represents a forced air cooling system [51], and shows visibly higher temperatures in the cell compared to other cooling levels. For an equivalent circulating pressure drop, a heat transfer coefficient of $340 \text{ W}/(\text{m}^2 \text{ K})$ was determined for a liquid cooled system by in-house tests.

Testing with cold plates found a forced air h value of about $150 \text{ W}/(\text{m}^2 \text{ K})$, and $1493 \text{ W}/(\text{m}^2 \text{ K})$ for liquid cooling for an equivalent pumping energy for circulating coolant. Two h values, one below and one above $340 \text{ W}/(\text{m}^2 \text{ K})$ (or surrounding $1493 \text{ W}/(\text{m}^2 \text{ K})$ for cold plates) were tested to determine the functionality of the applied cooling effort with ice plates or cold plates. These results are shown in Fig. 11. For US06 driving, and the standard polymer case material, it can be seen that for the ice plate system, a temperature rise in the cell of about 4 K occurs at $h = 85 \text{ W}/(\text{m}^2 \text{ K})$, but at higher h values, the temperature increase settles asymptotically to just under 2 K. When the coefficient h has a value upwards of $85 \text{ W}/(\text{m}^2 \text{ K})$, a liquid cooled system is represented. For all parameters the same, except using cold plates, the temperature increases can be seen to be about 30 K larger. Other trends observed are that the case materials have an effect. For equivalent simulations, cell temperatures decrease starting from the largest values with the polymer cases, followed by steel cases, aluminum cases and finally aluminum cases of $508 \mu\text{m}$ (double) thickness gave the lowest battery temperatures. The HWY drive cycles is less intense than the US06 drive cycle and also resulted in lower battery temperatures. There was not one scenario where a cold plate cooled system exceeded the performance of an ice plate cooled system.

In Fig. 12, the temperature gradient inside the cell is plotted as a function of the cooling effort, and compares cold plates used for battery cells with aluminum cases to ice plates used with battery cells with polymeric cases. In all cases the ice plate configuration shows a superior performance. The liquid cooling systems with ice plates are seen to be particularly effective, as the temperature gradients exist only slightly above the external cooling set point of 303 K. For the case of HWY drive

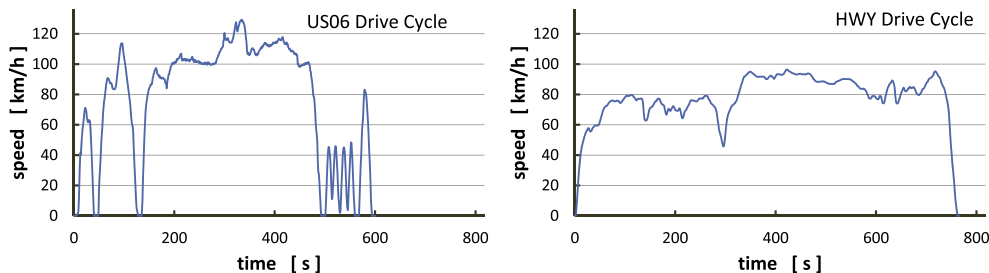


Fig. 6. Reference data for US06 and HWY drive cycles. From [50].

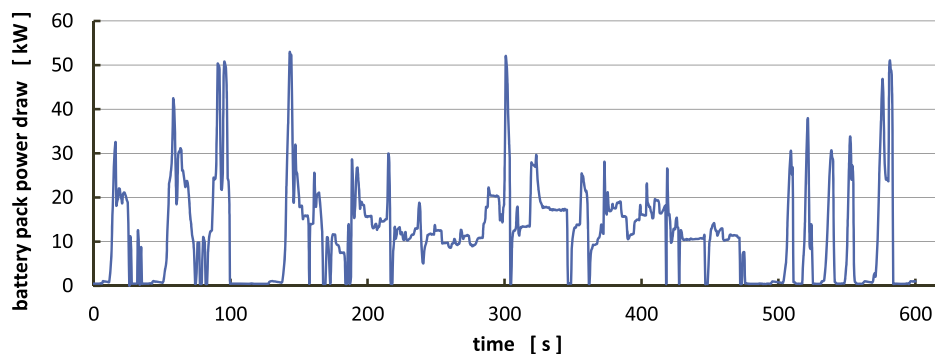


Fig. 7. In-house dynamometer data showing total power draw for the one bank of 96 cells subjected to a US06 drive cycle.

Table 2

Simulation parameters for determining time-temperature profiles. Battery life-time simulations were run for all the parameters outlined here, across the SOH range.

Parameter	Values
Drive cycle	US06, HWY
Cooling plate heat transfer coefficient h W/(m ² K)	ice plate: 35 (forced air), [85, 340, 510] (liquid cooling) cold plate: 150 (forced air), [373, 1493, 2240] (liquid cooling)
Battery case materials	ice plate: polymer pouch, aluminum cold plate: polymer pouch, steel aluminum, thick aluminum
%SOH (state-of-health)	100, 95, 90, 85, 80, 75, 70

cycle at an elevated cooling level, the cold plate system approaches ice plate performance in a general sense, but the temperature rise is still around double the amount of an ice plate system, although the magnitude is about 5 K. It can also be seen in Fig. 12-b, that battery cases with thicker aluminum reduce cell temperatures by about 1 K.

5.2. Battery degradation effects

As the battery is used and ages, lithium lost from cycling is deposited in the SEI layer which becomes steadily thicker over time.

The thermal overlays employed in the Kim-SPM are derived from the curves such as those plotted in Fig. 13 which shows average cell temperatures over the course of 50 km of both US06 and HWY drive cycles, for $h = 340 \text{ W/m}^2 \text{ K}$, which is the standard liquid cooled level for ice plates. Fig. 13 shows drive cycle thermal trajectories for a range of battery state of health (SOH) levels. The SOH parameter reflects the percent of remaining original capacity in a cell. Thus, 100% SOH is the value for a new cell, while, 90% SOH means that a cell has lost 10% of its starting capacity. Updates to the cell capacity loss is done numerically at each time step, where the degradation kinetics can be determined in a rigorous physically based and thermally dependant manner. The Fig. 13 curves were determined by Kim-SPM simulations with electrode lithium concentration states corresponding to the varying extents of lithium depletion along with SEI layer thicknesses for these states, for each SOH level where data were stored.

Additionally, time-temperature profiles were obtained at 95, 85 and 75% SOH, allowing better resolution for interpolating temperatures. Curve for these levels are not shown in Fig. 13.

5.3. Vehicle lifetime estimates

Kim-SPM simulations were conducted for the set of parameters

found in Table 2. The base case simulations were scenarios consisting of driving 50 km each day, by either US06 or HWY drive cycle, followed by a recharge at 6.6 kW (Level 2b). Simulations were run at cooling levels from $h = 35$ to $510 \text{ W}/(\text{m}^2 \text{ K})$ for ice plates. Fig. 14 is a plot showing cell capacity over time, with a 25% capacity loss (or 75% remaining capacity) level being considered as battery end of life. Here, end of life occurred after a time ranging between 5.4 and 8.1 years, according to cooling level and drive cycle.

In Fig. 14, the lifetime estimates do not vary much with cooling levels ranging from 85 through $510 \text{ W}/(\text{m}^2 \text{ K})$, which are all levels for a liquid cooling system. For a forced air cooling system however, ($h = 35 \text{ W}/(\text{m}^2 \text{ K})$) 50 km of daily US06 driving results in an end of life point at 5.36 years, close to two years less than with any level of liquid cooling. Of note, simulations run at a passive air cooling level of $h = 7 \text{ W}/(\text{m}^2 \text{ K})$ predicted a cell life of only 4.65 years under this same usage scenario.

SOH trajectories of the range of cooling levels for both US06 and HWY drive cycles for battery packs that are cooled by cold plates are shown in Fig. 15. In general, there is a loss of around 2 years of service life for US06 driving, and about 1 year of service life for HWY driving. These margins improve slightly with increased cooling level. For future second generation electric vehicles which are expected to have much larger energy capacities, driving at this intensity would allow longer battery pack lifetimes, to the point where what service life would be lost between ice and cold plate cooled systems could become acceptable.

6. Conclusions

The coupled electrochemical and thermal simulations with relevant usage scenarios performed on automotive batteries configured in packs with ice or cold plate liquid cooling systems, produced a novel and plausible context for evaluating the battery pack thermal state over its service lifetime.

The range of imposed conditions produced cell lifetime estimates from as short as 3.5 years, to beyond 8.1 years. Electric vehicles presently emerging on the market have larger cell capacities than the 30 Ah cell considered here, and thus lifetimes longer than those reported here could be expected, while still following trends shown by the parametric variations explored here.

Ice plate systems performed universally better in all situations, even with relatively insulating polymer cell cases were compared to more thermally conducting metal cell cases more suitable for cold plate systems. Lifetime estimates were made for a range of conditions and systems, and taken in context with their capital and operating costs, suitable cooling system configurations can now be selected with a better understanding of their relative merits and expected performance.

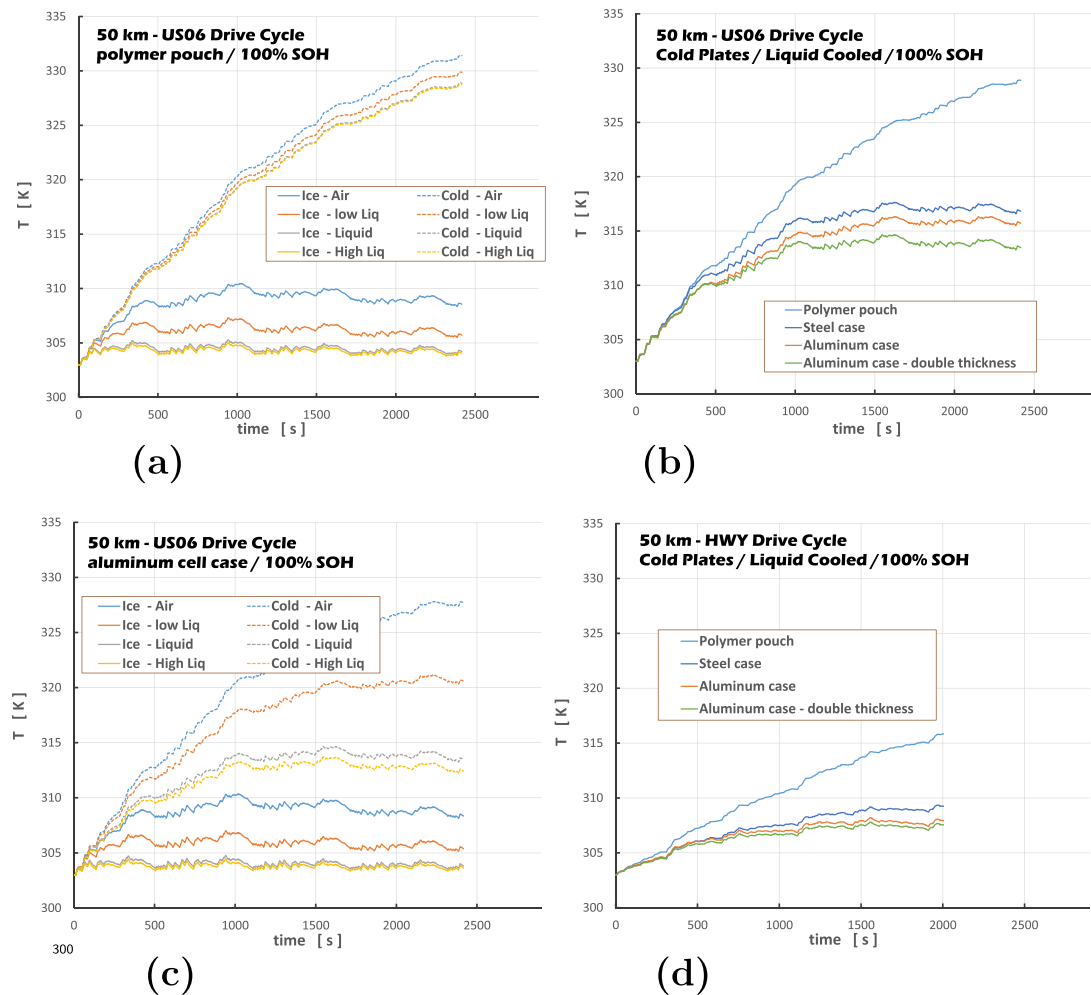


Fig. 8. Average cell temperatures over 50 km driving with 100% SOH batteries for various test scenarios: (a) US06 drive cycle, polymer cell case, ice and cold plates, air cooling and three levels of liquid cooling. (b) US06 drive cycle, liquid cooling, four different cell case materials. (c) US06 drive cycle, aluminum cell case, ice and cold plates, air cooling and three levels of liquid cooling. (d) HWY drive cycle, liquid cooling, four different cell case materials.

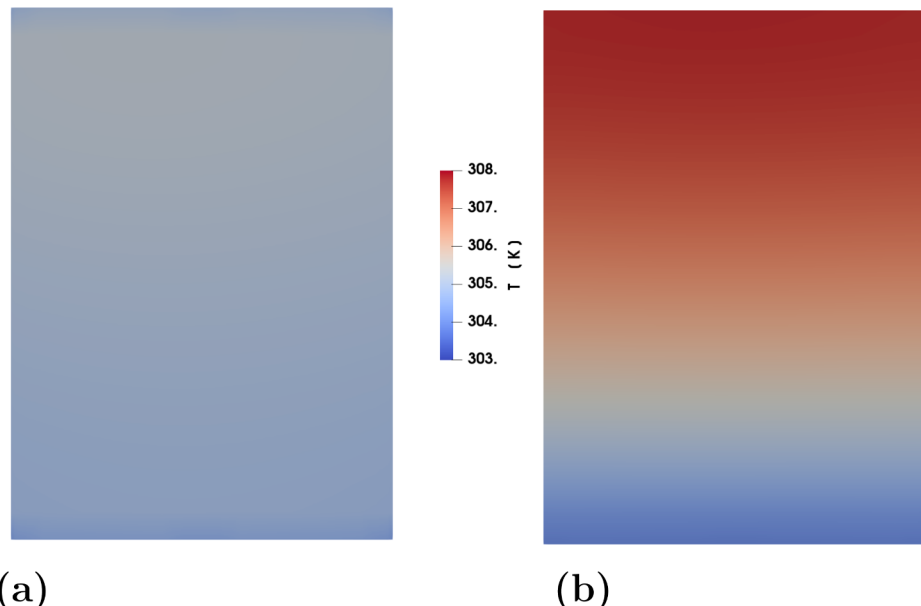


Fig. 9. Main-face section temperature distributions in operating cell at 125 s point of US06 drive cycle, for cells with polymer case and standard liquid cooling. (a) ice plate. (b) cold plate.

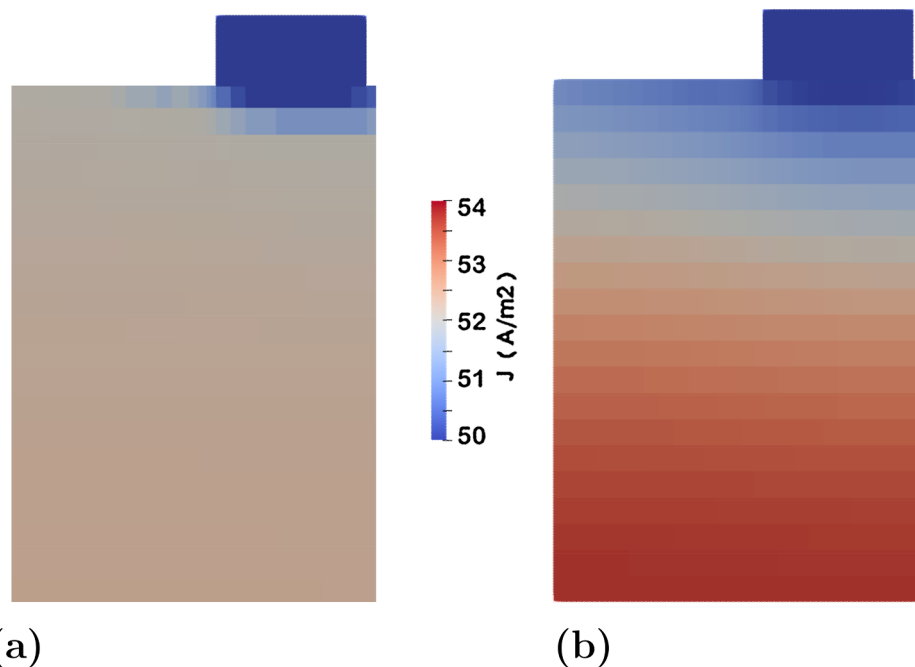


Fig. 10. Main-face section current distributions in operating cell at 125 s point of US06 drive cycle, for cells with polymer case and standard liquid cooling. (a) ice plate. (b) cold plate.

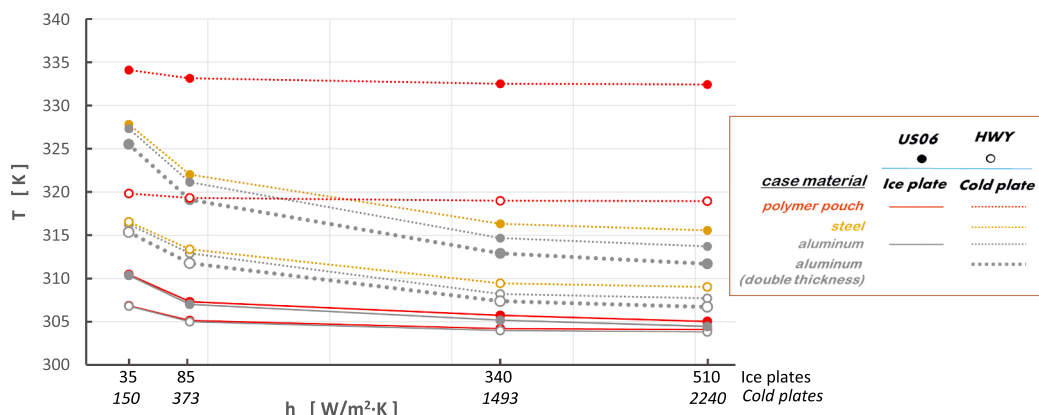


Fig. 11. Maximum cell temperature over 50 km driving as function of cooling effort for US06 and HWY drive cycles simulated with various battery cell case materials.

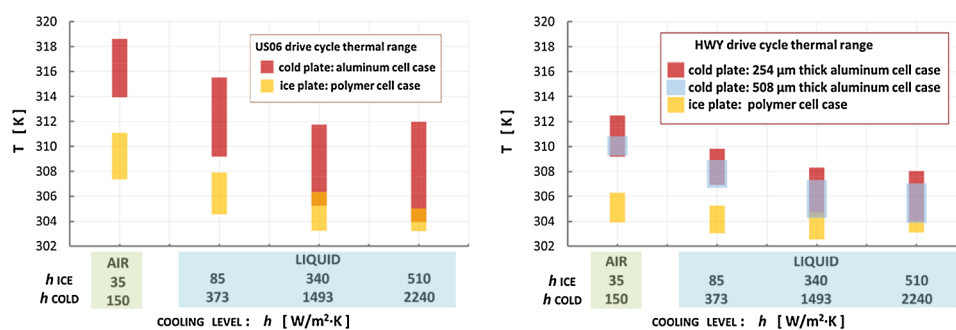


Fig. 12. Comparison of cold plate cooled and ice plate cooled temperature ranges inside battery cells versus cooling effort. (a) US06 drive cycle. (b) HWY drive cycle.

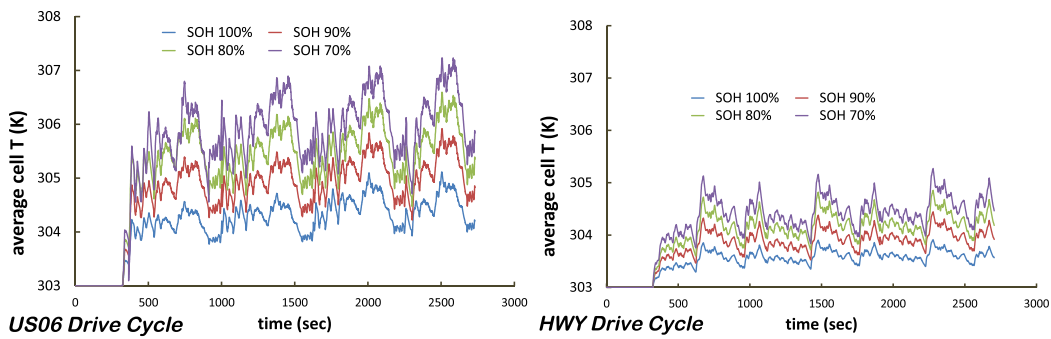


Fig. 13. Average cell temperatures over 50 km driving for US06 (left) and HWY (right) drive cycles, with ice plate cooling level $h = 340 \text{ W/m}^2 \text{ K}$ for various levels of SOH. Battery cell cases were polymer pouch material.

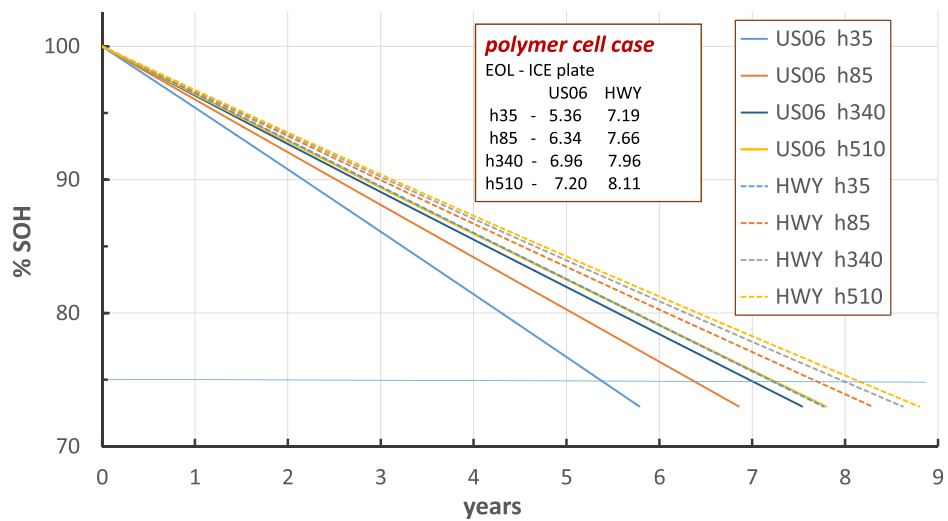


Fig. 14. Effect of cooling with ice plate configuration with a polymer battery case. Plot shows battery %SOH versus time for daily 50 km of US06 and HWY driving. Cooling levels ranging from at $h = 35 \text{ W}/(\text{m}^2 \text{ K})$ to $510 \text{ W}/(\text{m}^2 \text{ K})$.

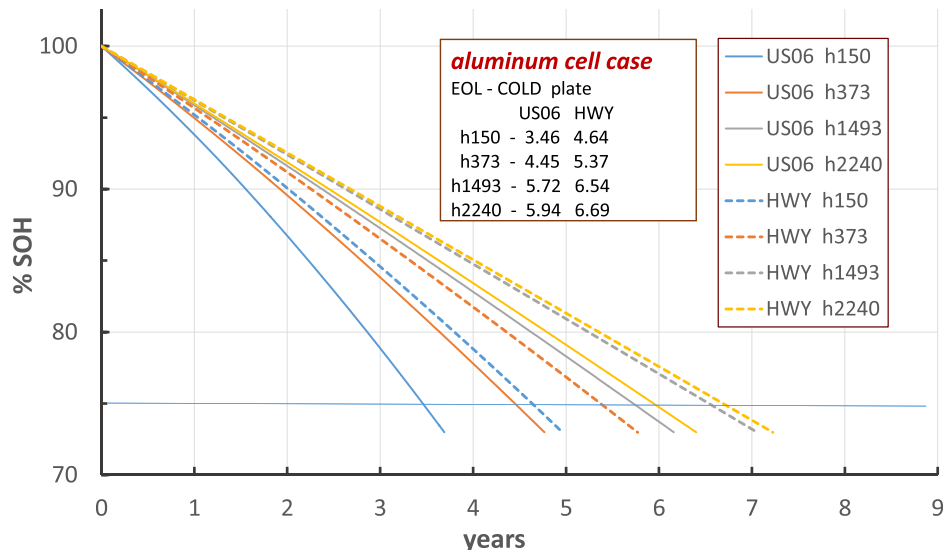


Fig. 15. Effect of cooling with cold plate configuration with an aluminum battery case. Plot shows battery %SOH versus time for daily 50 km of US06 and HWY driving. Cooling levels ranging from at $h = 150 \text{ W}/(\text{m}^2 \text{ K})$ to $2240 \text{ W}/(\text{m}^2 \text{ K})$.

Acknowledgements

The authors would like to thank Aaron Loiselle-Lapointe from Environment Canada for providing EV test data for calibrating the battery model. Funding for this work was provided through the

Program of Energy Research and Development at Natural Resources Canada, and the project was commissioned by the Vehicle Propulsion Technology program of the National Research Council of Canada.

Appendix A. Supplementary material

Supplementary data associated with this article can be found, in the online version, at <https://doi.org/10.1016/j.aplthermaleng.2019.03.146>.

References

- [1] M.A. Hannan, F.A. Azidin, A. Mohamed, Hybrid electric vehicles and their challenges: a review, *Renew. Sustain. Energy Rev.* 29 (2014) 135–150.
- [2] M. Yilmaz, P.T. Krein, Review of battery charger topologies, charging power levels, and infrastructure for plug-in electric and hybrid vehicles, *IEEE Trans. Power Electron.* 28 (5) (2013) 2151–2169.
- [3] A. Barré, B. Deguilhem, S. Grolleau, M. Gérard, A review on lithium-ion battery ageing mechanisms and estimations for automotive applications, *J. Power Sources* 241 (2013) 680–689.
- [4] L. Lu, X. Han, J. Li, J. Hua, M. Ouyang, A review on the key issues for lithium-ion battery management in electric vehicles, *J. Power Sources* 226 (2013) 272–288.
- [5] K. Darcovich, D.D. MacNeil, S. Recoskie, B. Kenney, Coupled electrochemical and thermal battery models for thermal management of prismatic automotive cells, *Appl. Therm. Eng.* 133 (2018) 566–575.
- [6] K. Darcovich, D.D. MacNeil, S. Recoskie, Q. Cadic, F. Ilinca, B. Kenney, Coupled numerical approach for automotive battery pack lifetime estimates with thermal management, *J. Electrochem. Energy Convers. Storage* 15 (2) (2018) 021004–1–021004–12.
- [7] J. Kim, J. Oh, H. Lee, Review on battery thermal management system for electric vehicles, *Appl. Therm. Eng.* 149 (2019) 192–212.
- [8] A. Jarrett, I.Y. Kim, Design optimization of electric vehicle battery cooling plates for thermal performance, *J. Power Sources* 196 (2011) 10359–10368.
- [9] H. Teng, K. Yeow, Design of direct and indirect liquid cooling systems for high-capacity, high-power lithium-ion battery packs, *SAE Int. J. Alt. Powertrains* 1 (2) (2012) 525–536.
- [10] E. Yen, K.-H. Chen, T. Han, B. Khalighi, Application of CAEBAT Full Field Approach for a Liquid-Cooled Automotive Battery Pack, *SAE Technical Paper* 2016-01-1217, SAE 2016 World Congress and Exhibition, Detroit, MI, USA, April 12–14, 2016.
- [11] S. Panchal, I. Dincer, M. Agelin-Chaab, R. Fraser, M. Fowler, Transient electrochemical heat transfer modeling and experimental validation of a large sized LiFePO₄/graphite battery, *Int. J. Heat Mass Transf.* 109 (2017) 1239–1251.
- [12] S. Panchal, M. Akhoundzadehr, K. Raahemifar, M. Fraser, R.M. Fowler, Heat and mass transfer modeling and investigation of multiple LiFePO₄/graphite batteries in a pack at low C-rates with water-cooling, *Int. J. Heat Mass Transf.* 135 (2019) 368–377.
- [13] A. Jarrett, I.Y. Kim, Influence of operating conditions on the optimum design of electric vehicle battery cooling plates, *J. Power Sources* 245 (2014) 644–655.
- [14] H. Sun, X. Wang, B. Tossan, R. Dixon, Three-dimensional thermal modeling of a lithium-ion battery pack, *J. Power Sources* 206 (2012) 349–356.
- [15] A. Moradikazerouni, M. Afrand, J. Alsarraf, O. Mahian, S. Wongwises, M.D. Tran, Comparison of the effect of five different entrance channel shapes of a micro-channel heat sink in forced convection with application to cooling a supercomputer circuit board, *Appl. Therm. Eng.* 150 (2019) 1078–1089.
- [16] Y. Li, Z. Zhou, W.T. Wu, Three-dimensional thermal modeling of Li-ion battery cell and 50 V Li-ion battery pack cooled by mini-channel cold plate, *Appl. Therm. Eng.* 147 (2019) 829–840.
- [17] W. Tong, K. Somasundaram, E. Birgersson, A.S. Mujumdar, C. Yap, Numerical investigation of water cooling for a lithium-ion bipolar battery pack, *Int. J. Therm. Sci.* 94 (2015) 259–269.
- [18] J. Wang, Y. Gan, J. Liang, M. Tan, Y. Li, Sensitivity analysis of factors influencing a heat pipe-based thermal management system for a battery module with cylindrical cells, *Appl. Therm. Eng.* 151 (2019) 475–485.
- [19] S. Basu, K.S. Hariharan, S.M. Kolake, T. Song, D.K. Sohn, T. Yeo, Coupled electrochemical thermal modelling of a novel Li-ion battery pack thermal management system, *Appl. Energy* 181 (2016) 1–13.
- [20] M. Malik, I. Dincer, M.A. Rosen, M. Mathew, M. Fowler, Thermal and electrical performance evaluations of series connected Li-ion batteries in a pack with liquid cooling, *Appl. Therm. Eng.* 129 (2018) 472–481.
- [21] D.R. Weber, R.M. Brisbane, Cooling plate for lithium-ion battery pack, US Patent US 2015/0044523 A1, 12 February 2015, 9 pp.
- [22] N. Bachmann, J. Meintschel, D. Schröter, Battery (e.g. high-power or high-voltage batteries) has cooling device and intermediate frame that are connected with output conductor of individual battery cells, German Patent DE 10 2012 018113 A1, 13 March 2014, 14 pp.
- [23] B. Boddakayala, Cooling system for vehicle batteries, US Patent US 2013/0183555 A1, 18 July 2013, 16 pp.
- [24] S. Nicholls, Vehicle battery pack, a system for cooling a battery pack and a cooling plate for use in the system, US Patent US 2015/0140366 A1, 21 May 2015, 30 pp.
- [25] A. Betz, J. Helber, G. Johannotkraix, F. Maier, M. Meier, N. Winterholler, Floor plate for a battery, in particular a traction battery, and the traction battery, German Patent DE 10 2016 008110 A1, 23 February 2017, 10 pp.
- [26] K. Smith, E. Wood, S. Santhanagopalan, G.-H. Kim, A. Pesaran, Advanced Models and Controls for Prediction and Extension of Battery Lifetime, *Advanced Automotive Battery Conference*, Atlanta, GA, USA, February 4–6, 2014.
- [27] V. Marano, S. Onori, Y. Guezennec, G. Rizzoni, N. Madella, Lithium-ion batteries life estimation for plug-in hybrid electric vehicles, *IEEE Vehicle Power and Propulsion Conference*, Dearborn, MI, USA, September 7–11, 2009, pp. 536–543.
- [28] B. Lunz, Z. Yan, J.B. Gerschler, D.U. Sauer, Influence of plug-in hybrid electric vehicle charging strategies on charging and battery degradation costs, *Energy Policy* 46 (2012) 511–519.
- [29] S.B. Peterson, J. Apt, J.F. Whitacre, Lithium-ion battery cell degradation resulting from realistic vehicle and vehicle-to-grid utilization, *J. Power Sources* 195 (8) (2010) 2385–2392.
- [30] K. Darcovich, S. Recoskie, H. Ribberink, F. Pincet, A. Foissac, Effect on battery life of vehicle-to-home electric power provision under Canadian residential electrical demand, *Appl. Therm. Eng.* 114 (2017) 1515–1522.
- [31] G. Ning, B.N. Popov, Cycle life modeling of lithium-ion batteries, *J. Electrochem. Soc.* 151 (2004) A1584–A1591.
- [32] S.K. Rahimian, S.C. Rayman, R.E. White, Comparison of single particle and equivalent circuit analog models for a lithium-ion cell, *J. Power Sources* 196 (20) (2011) 8450–8462.
- [33] S.K. Rahimian, S.C. Rayman, R.E. White, Optimal charge rates for a lithium ion cell, *J. Power Sources* 196 (2011) 10297–10304.
- [34] M. Guo, G. Sikha, R.E. White, Single-particle model for a lithium-ion cell: thermal behavior, *J. Electrochem. Soc.* 158 (2011) A122–A132.
- [35] M. Doyle, J. Newman, A.S. Gozdz, C.N. Schmutz, J.-M. Tarascon, Comparison of modeling predictions with experimental data from plastic lithium ion cells, *J. Electrochem. Soc.* 143 (1996) 1890–1903.
- [36] K.H. Kwon, C.B. Shin, T.H. Kang, C.S. Kim, A two-dimensional modeling of a lithium-polymer battery, *J. Power Sources* 163 (1) (2006) 151–157.
- [37] U.S. Kim, C.B. Shin, C.S. Kim, Effect of electrode configuration on the thermal behavior of a lithium-polymer battery, *J. Power Sources* 180 (2) (2008) 909–916.
- [38] U.S. Kim, C.B. Shin, C.S. Kim, Modeling for the scale-up of a lithium-ion polymer battery, *J. Power Sources* 189 (1) (2009) 841–846.
- [39] U.S. Kim, J. Yi, C.B. Shin, T. Han, S. Park, Modelling the thermal behaviour of a lithium-ion battery during charge, *J. Power Sources* 196 (11) (2011) 5115–5121.
- [40] L.O. Valoen, J.N. Reimers, Transport properties of LiPF₆-based Li-ion battery electrolytes, *J. Electrochem. Soc.* 152 (5) (2005) A882–A891.
- [41] B. Kenney, K. Darcovich, D.D. MacNeil, I.J. Davidson, Modelling the impact of variations in electrode manufacturing on lithium-ion battery modules, *J. Power Sources* 213 (2012) 391–401.
- [42] K. Kumaresan, G. Sikha, R.E. White, Thermal model for a Li-ion cell, *J. Electrochem. Soc.* 155 (2) (2008) A164–A171.
- [43] B. Wu, V. Yufit, M. Marinescu, G. J. Offer, R.F. Martinez-Botas, N.P. Brandon, Coupled thermal electrochemical modelling of uneven heat generation in lithium-ion battery packs, *J. Power Sources* 243 (2013) 544–554.
- [44] G. Li, S. Li, Physics-based CFD simulation of lithium-ion battery under the FUDS driving cycle, *ECS Trans.* 64 (33) (2015) 1–14.
- [45] J. Yi, U.S. Kim, C.B. Shin, T. Han, S. Park, Three-dimensional thermal modeling of a lithium-ion battery considering the combined effects of the electrical and thermal contact resistances between current collecting tab and lead wire, *J. Electrochem. Soc.* 160 (3) (2013) A437–A443.
- [46] F. Cverna (Ed.), ASM ready reference: thermal properties of metals, ASM International, 2002, p. 560.
- [47] I.T. Yun, L.G. Chem, Product Specification, Rechargeable Lithium Ion Battery, Model: ICR18650S2 2200mA, January 2003, 8 pp.
- [48] F.R. Kalhammer, B.M. Kopf, D.H. Swan, V.P. Roan, M.P. Walsh, Status and prospects for zero emissions vehicle technology, Report of the ARB Independent Expert Panel, State of California Air Resources Board, 2007, 207 pp.
- [49] T. Maric, J. Hopken, K. Mooney, The OpenFOAM technology primer, Sourceflux Publ., Duisburg, 2014, pp. 455.
- [50] <https://www.epa.gov/vehicle-and-fuel-emissions-testing>, update of March 24, 2016.
- [51] X.M. Xu, R. He, Research on the heat dissipation performance of battery pack based on forced air cooling, *J. Power Sources* 240 (2013) 33–41.